Spatiotemporal changes of seismic attenuation caused by injected CO_2 at the Frio-II pilot site, Dayton, TX, USA

Tieyuan Zhu

Jonathan B. Ajo-Franklin

Thomas M. Daley
First published: 18 August 2017
https://doi.org/10.1002/2017JB014164
Cited by: 2
UC-eLinks

Abstract

A continuous active source seismic monitoring data set was collected with crosswell geometry during CO_2 injection at the Frio-II brine pilot, near Liberty, TX. Previous studies have shown that spatiotemporal changes in the *P* wave first arrival time reveal the movement of the injected CO_2 plume in the storage zone. To further constrain the CO_2saturation, particularly at higher saturation levels, we investigate spatial-temporal changes in the seismic attenuation of the first arrivals. The attenuation changes over the injection period are estimated by the amount of the centroid frequency shift computed by local time-frequency analysis. We observe that (1) at receivers above the injection zone seismic attenuation does not change in a physical trend; (2) at receivers in the injection zone attenuation sharply increases following injection and peaks at specific points varying with distributed receivers, which is consistent with observations from time delays of first arrivals; then, (3) attenuation decreases over the injection time. The attenuation change exhibits a bell-shaped pattern during CO_2 injection. Under Frio-II field reservoir conditions, White's patchy saturation model can quantitatively explain both the *P* wave velocity and attenuation response observed. We have combined the velocity and attenuation change data in a crossplot format that is useful for model-data comparison and determining patch size. Our analysis suggests that spatial-temporal attenuation change is not only an indicator of the movement and saturation of CO_2 plumes, even at large saturations, but also can quantitatively constrain CO_2 plume saturation when used jointly with seismic velocity.

Plain Language Summary

Geological CO_2 storage is a promising approach to meet the urgent need of reducing anthropogeic CO_2 emissions into the atmosphere. One key component required for geologic

CO_2 sequestration is the monitoring of subsurface CO_2 migration and distribution; monitoring is a crucial tool for refining subsurface flow models, verifying CO_2 containment, and tracking any leaks before they impact groundwater or terrestrial environments. We observed field-scale spatiotemporal seismic attenuation changes from crosswell continuous active source seismic monitoring data during CO_2 injection. We found that seismic attenuation is not only an indicator of the movement and saturation of CO_2plumes, even at large saturations, but also can quantitatively constrain CO_2 plume saturation when used jointly with seismic velocity.

1 Introduction

Geological CO_2 storage is a promising approach to meet the urgent need of reducing anthropogeic CO_2 emissions into the atmosphere. One key component required for geologic CO_2 sequestration is the monitoring of subsurface CO_2 migration and distribution; monitoring is a crucial tool for refining subsurface flow models, verifying CO_2 containment, and tracking any leaks before they impact groundwater or terrestrial environments. Time-lapse seismic imaging has been shown to be an effective technique for subsurface CO_2 monitoring for both enhanced oil recovery [*Lazaratos and Marion*, 1997; *Majer et al*., 2006; *White*, 2013] and sequestration [*Arts et al*., 2004; *Xue et al*., 2006*; Daley et al*., 2008; *Gareth and Chadwick*, 2012; *Ajo-Franklin et al*., 2013]. For example, time-lapse crosswell tomographic velocity estimates of the Frio-I CO_2 plume demonstrated a seismic velocity decrease up to 500 m/s within the plume that were caused by the injection of supercritical CO_2 into the brine reservoir [*Hovorka et al*., 2006; *Ajo-Franklin et al*., 2007; *Daley et al*., 2007; *Al Hosni et al*., 2016]. For the expected advanced role of monitoring in the future, e.g., for the accounting of CO_2 emissions [*Benson*, 2006], there is a demand for seismic monitoring to provide early detection of leaks and quantitative estimation of the amount of CO_2 in the storage zone. However, current active source seismic monitoring approaches are limited by sparse temporal sampling, dictated by the high cost of repeat surveys.

A new monitoring system, referred to as continuous active source seismic monitoring (CASSM), was developed and tested in the small-scale Frio site to provide continuous monitoring of injected CO_2 [*Daley et al*., 2007] using a semipermanently deployed downhole source and an array of hydrophones. The primary information currently extracted from the CASSM data is delay time (change in crosswell traveltime) as a function of calendar time [*Daley et al*., 2007, 2011]. Results, analyzed as the change in traveltime recorded at various depths in a nearby observation well, allowed hour-by-hour monitoring of the growing CO_2 plume via the induced seismic velocity change. Traveltime changes of 0.2 to 1.0 ms (up to 6%) were observed, with no change seen at control sensors placed above the reservoir. The traveltime measurements indicate that the CO_2 plume reached the top of the reservoir sand before reaching the observation well, where regular fluid sampling was occurring during the injection, thus providing

information about the in situ buoyancy of CO_2 and constraining reservoir flow models [*Daley et al*., 2011].

Rock physics studies have observed that significant reductions in *P* wave velocity can occur at small CO_2 saturations [e.g., *Carcione et al*., 2006; *Xue et al*., 2009*; Nakagawa et al*., 2013] due to the highly compressible nature of the supercritical CO_2 ($scCO_2$) phase at reservoir conditions. This phenomenon can provide a basis for monitoring CO_2 leakage using seismic velocity. It enables us to detect CO_2 leakage at the earlier stage because a small amount of leaked CO_2can change the seismic velocity. However, *P* wave velocity has been theoretically and experimentally found to be relatively insensitive to CO_2 saturation at higher saturation levels, particularly at surface seismic frequencies [*Chadwick et al*., 2005; *Carcione et al*., 2006; *Lei and Xue*, 2009; *Xue et al*., 2009]; prior rock physics model evaluations at realistic site conditions [e.g., *Lumley et al*., 2008; *Ajo-Franklin et al*., 2013] have shown minimal *P* wave velocity sensitivity to CO_2 saturation past 10–20%, suggesting that seismic velocity must be augmented with other recoverable parameters to constrain this saturation regime.

In contrast, seismic attenuation is observed to be at a maximum at partial saturation [*Winkler and Nur*, 1982; *Nakagawa et al*., 2013] and is still sensitive to large gas saturations 30–50% [*Carcione et al*., 2006; *Lei and Xue*, 2009; *Azuma et al*., 2014; *Caspari et al*., 2014]. Few field studies have attempted to utilize *Q* to assist in CO_2 saturation estimates due to the challenges of reliable estimation from conventional seismic monitoring data sets. The crosswell CASSM data set acquired as part of the Frio-II pilot is the ideal candidate for such an attenuation study due to the highly repeatable active source and small-scale sequestration site.

In this study, we investigate spatiotemporal attenuation changes of the first *P* wave arrival signals collected during the Frio-II CO_2 field pilot, documented in *Daley et al*. [2007]. The high-quality first arrivals transmitted through the CO_2 saturated area are chosen for attenuation analysis. Spatial distribution of attenuation is obtained with wide aperture source-sensor pairs. Temporal attenuation change over the 60 h is measured relative to preinjection. The calculation of attenuation starts with data stacking and isolating the first arrival. The centroid frequency of the first arrival is computed by the local frequency tool with stabilized regularization [*Liu et al*., 2011]. Finally, using the theory of centroid frequency shift, the predicted centroid frequency shifts can be converted to attenuation changes [*Quan and Harris*, 1997]. To explain how attenuation changes correlate with the amount of CO_2 (saturation), we employ White's attenuation model with two selected patch sizes [*White*, 1975; *Dutta and Seriff*, 1979].

The paper is organized as follow. We first review the field setup of continuous crosswell seismic monitoring and traveltime observation. We then step through a processing workflow for extracting temporal seismic attenuation change, with sections devoted to theory of temporal attenuation change using centroid frequency shift and robustness analysis in attenuation changes. Finally, in combination with White's rock physics model, we interpret spatiotemporal attenuation changes in terms of the variation of patchy size and scCO_2saturation during injection.

2 Background and Methodology

2.1 Frio-II Field Site and Monitoring Data

We studied a crosswell seismic monitoring data set from the Frio-II brine pilot site. The Frio-II project was a small-scale injection of supercritical CO_2 into a high permeability reservoir at the same site as the larger Frio-I test in southeast Texas, USA [*Hovorka et al*., 2006]. About 380 t of CO_2 were injected into the Blue sand of the Frio formation. The fluvial Blue sand is at a depth of 1657 m, is 17 m thick, and has a dip of 18°, with about 30% porosity and permeability of 1 to over 4 darcies.

The experiment site had two wells, 30 m apart, a down-dip injector and a dedicated, updip, observation well. In the observation well, a 24 hydrophone array was deployed with 13 functioning and analyzed in this study. The sensor locations included depths above and below a packer (five above the packer and eight below). The packer was deployed at the top of the reservoir sand and above well casing perforations, as shown in Figure 1a.

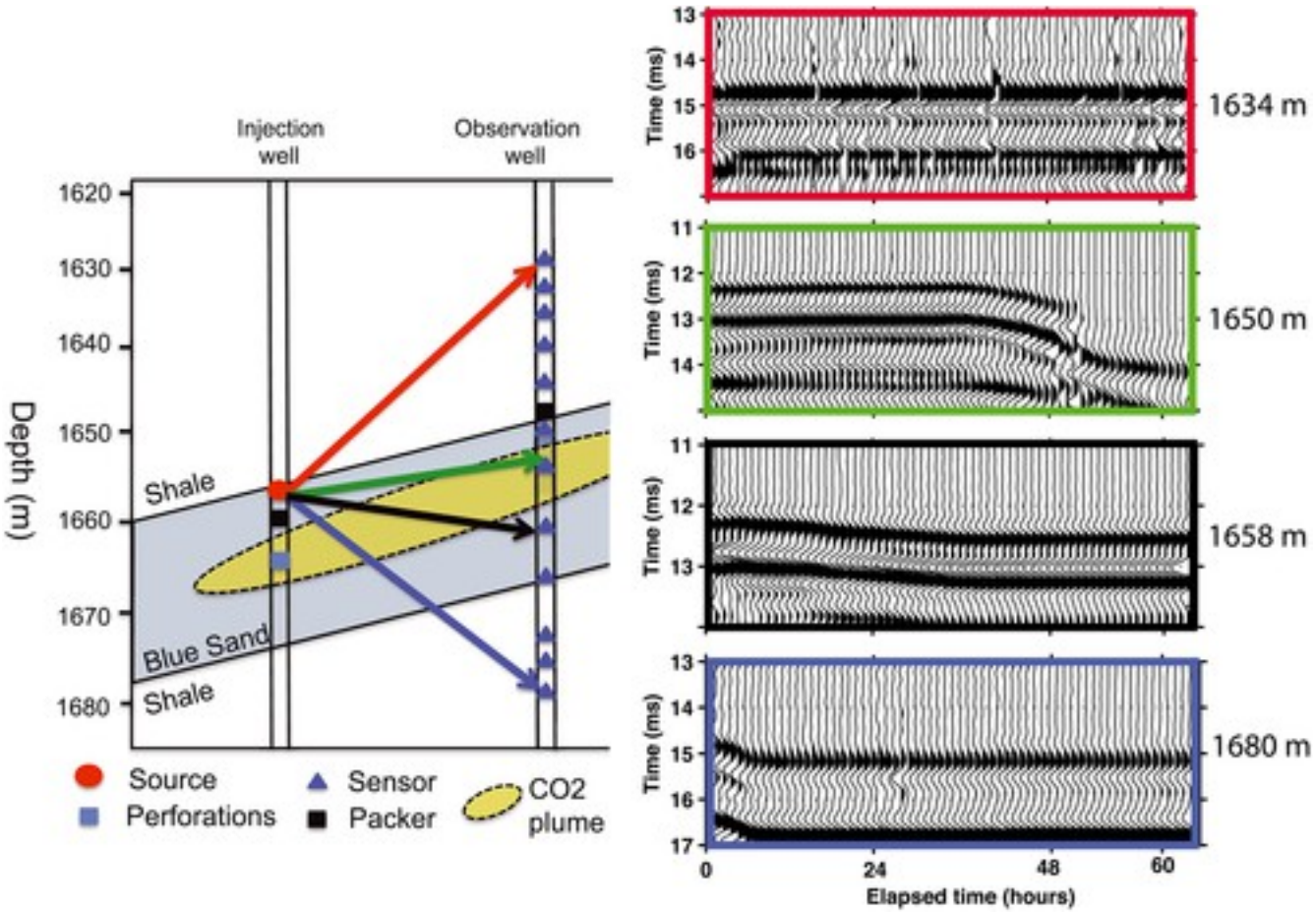

Figure 1

Open in figure viewerPowerPoint

(a) Sketch of geometry of active source seismic crosswell monitoring in the Frio brine pilot site. (b) Seismic traces at four receivers as a function of the calendar time after CO_2 injection. Each seismic trace is the result of stacking 15 min of seismic data.

Caption

Crosswell CASSM uses a fixed location source and fixed location sensors in boreholes to continuously monitor seismic waveforms as they are modified by injecting CO_2 [*Daley et al*., 2007]. CO_2 injection began at approximately 7:30 P.M., central daylight time, on 25 September 2006. About 60 h of continuous monitoring of crosswell seismic response provided information on the spatial and temporal variations of the CO_2 plume as it migrated updip, driven by buoyancy, across different raypaths between source-receiver pairs (Figure 1).

To enhance the signal-to-noise ratio (SNR) of the individual source pulse data, we stacked the pulse recordings in sets of 3600 (originally four pulses per second). Further stacking leads to a series of full seismic data gathers sampled at approximately 15 min intervals during the injection. Prior studies by *Silver et al*. [2007] have shown that the SNR improvement for vertical stacking extends to upward of 10^4 pulses using a highly repeatable piezoelectric source. The partial

section of the stacked seismic data at four different receivers is shown in Figure 1b. In the previous studies [*Daley et al*., 2007, 2011], delay time (change in crosswell traveltime) as a function of the calendar time was extracted from the CASSM data. As seen in Figure 1b, the different raypaths show different traveltime characteristics of the first arrival in both the magnitude of traveltime and the time of change. Notable is the large traveltime change observed on the 1650 m sensor (at the top of the reservoir) and the near zero delay-time change seen on the 1634 m sensor in the shale caprock (because the shale unit is relatively impermeable and CO_2 is not expected to migrate up). These CASSM data are ideal for constraining the modeled spatiotemporal evolution of the CO_2 plume [*Daley et al*., 2011].

2.2 Measuring Attenuation Using the Centroid Frequency Shift

In this study, we analyze seismic attenuation changes over a 60 h period during CO_2 injection. Seismic attenuation is measured by using the centroid frequency (CF) shift [*Quan and Harris*, 1997]. We focused on the first arrivals of crosswell seismic data. We used a local frequency technique to compute the CF map of the first arrival energy, following the approach described by *Liu et al*. [2011]. The centroid frequency at a given time is defined as

$$f_{cf}(t) = \frac{\int fF(t,f)df}{\int F(t,f)df}, \quad (1)$$

where $F(t,f)$ is the time-frequency map defined by time-varying Fourier coefficients constrained by shaping regularization [*Fomel*, 2007; *Liu et al*., 2011], t is the trace time, and f is the frequency. For each seismic trace, we will obtain a CF curve $f_{cf}(t)$ with respect to t. Then the maximum CF value of each trace $f_{mcf} = \max[f_{cf}(t)]$ is picked. We define the temporal variation of the CF with the calendar time T as $f_{mcf}(T)$.

Following the theory of the centroid frequency shift [*Quan and Harris*, 1997], we define attenuation coefficient α_0 along the raypath (distance is d) between a source and a receiver. It is written as

$$\alpha_0 d = \frac{f^S_{mcf} - f^R_{mcf}}{\sigma_S^2}, \quad (2)$$

where f^S_{mcf} and f^R_{mcf} are the CF of the signals at source and receivers. The variance σ_S^2 of source signal $S(t, f)$ is defined [*Quan and Harris*, 1997] as

$$\sigma_S^2 = \frac{\int \left(f - f^S_{cf}\right)^2 S(t,f)df}{\int S(t,f)df}. \quad (3)$$

Similarly, the variance σ_R^2 of receiver signal $F(t, f)$ is defined as

$$\sigma_R^2 = \frac{\int \left(f - f_{cf}^R\right)^2 F(t,f)df}{\int F(t,f)df}. \quad (4)$$

In practice, the source signature is not available, but it is the same for all receivers so we chose a reference value for all receivers. For example, we chose the mean value of receiver variance σ_R^2 at the top receiver (least disturbed) in the calculations below. It would not affect the attenuation changes among all receivers, though it might result in errors to the absolute attenuation changes within a single receiver. At a specific receiver, we assume that the raypath is a straight ray over the injection time since the velocity change is small (several percent) and *d* remains unchanged or slightly changes (this change is no larger than ~0.19% from our calculations of raylength by solving the eikonal solver using simulated time-lapse seismic velocity models given by the reservoir simulation [*Daley et al*., 2011]). We assume that the centroid frequency of the source is identical due to high repeatability of the source; i.e., f_{mcf}^S remains constant as a function of time. At the same receiver, therefore, temporal attenuation changes $\Delta\alpha$ caused by CO_2 injection is defined as

$$\Delta\alpha(T) = \frac{f_{mcf}^R(T) - f_{mcf}^R(0)}{d\sigma_s^2}, \quad (5)$$

where $\Delta\alpha(T) = \alpha_T - \alpha_0$ is the relative attenuation change to α_0, α_T is the attenuation at current injection (calendar) time *T*, and α_0 is the attenuation before CO_2 injection.

An example of an unprocessed seismic waveform is shown in Figure 2a, which depicts a temporal gather, a single source/receiver pair displayed as a function of time, at a depth of 1680 m over the period 60 h after injection. Significant reductions in apparent velocity are visible after injection while an amplitude shift can be seen after 40 h injection. Figure 2b shows the first arrivals selected by a 3 ms length Gaussian window. With prior tests, the 80-point smoothing window required by regularization [*Fomel*, 2007] gives sufficient resolution in the time and frequency when computing the time-frequency distribution. Figure 2c shows the centroid frequency map for the first arrivals in Figure 2b. The main frequencies are distributed along the first arrivals. Outside the area of the first arrivals, frequencies are not zero but less than 900 Hz. As shown in Figure 2c, high frequencies are measured during the first 6 h of injection and then have a significant reduction in amplitude between 6 and 15 h, and seem to gradually recover with a transition at around 40 h. We see that the trough of the centroid frequency at around 10 h corresponds to the largest time delay [*Daley et al*., 2007], as observed in Figure 2d, showing temporal variation of the CF with calendar time *T*:$f_{mcf}(T)$.

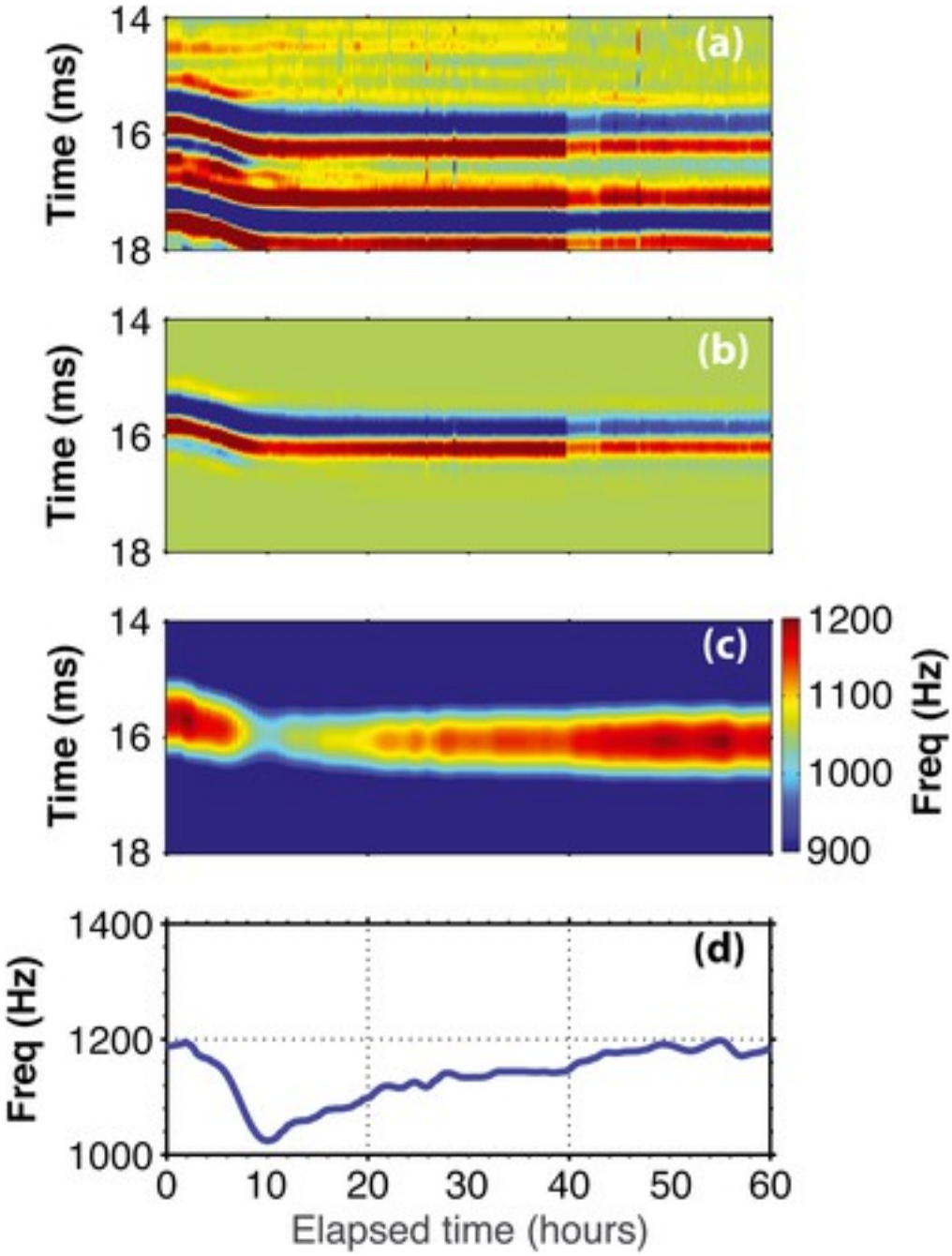

Figure 2

Open in figure viewerPowerPoint

CASSM data recorded at the depth of 1680 m and its centroid frequency map. (a) Unprocessed data; (b) first arrivals data windowed by a 3 ms length Gaussian window; (c) the centroid frequency map of Figure 2b; (d) the maximum centroid frequency value at each time. The horizontal axis represents elapsed calendar time with respect to the beginning of injection.

Caption

2.3 Robustness of the Workflow

To examine the robustness of the calculation of the CF values, we investigate two subjective factors: the duration of vertical stacking and the window length for selecting the first arrival.

2.4 Choice of Data Stacking

In the first experiment, we compared three scenarios' waveforms: 5 min stack, 15 min stack, and 30 min stack (Figure 3). Secondary input parameters are kept same as the above. Increased stacking time will increase the signal-to-noise ratio but reduce the temporal sampling. For example, at 2.5 h, waveform from 5 min stack is noisier than that from 15 min stack and 30 min stack, presumably due to rapid change in $scCO_2$ distribution. The 15 min stack is close to the 30 min stack in all time periods. In the majority of the periods in the experiment, the waveform variation between the three stacking intervals is slight. The advantage of selecting the 15 min stacking interval is improved S/N on the *P* arrival which enables more accurate traveltime determination. Similar observations with additional time-frequency analysis can also be seen from Figure 4. In the first row of Figure 4, three stacked seismograms do not appear different to casual inspection. In the second row, the first arrivals of three seismograms are windowed. The third row displays the CF maps of the three scenarios which exhibit a similar trend (high-low-high) but with some distinguishing features. For instance, the CF content of the first arrival for 5 min stack (left plot in the third row in Figure 4) seems noisy (temporal resolution) after 10 h, while the 30 min stacking seems too smooth to preserve temporal resolution. We see that the stacking duration influences the absolute values of the centroid frequency but not relative trend.

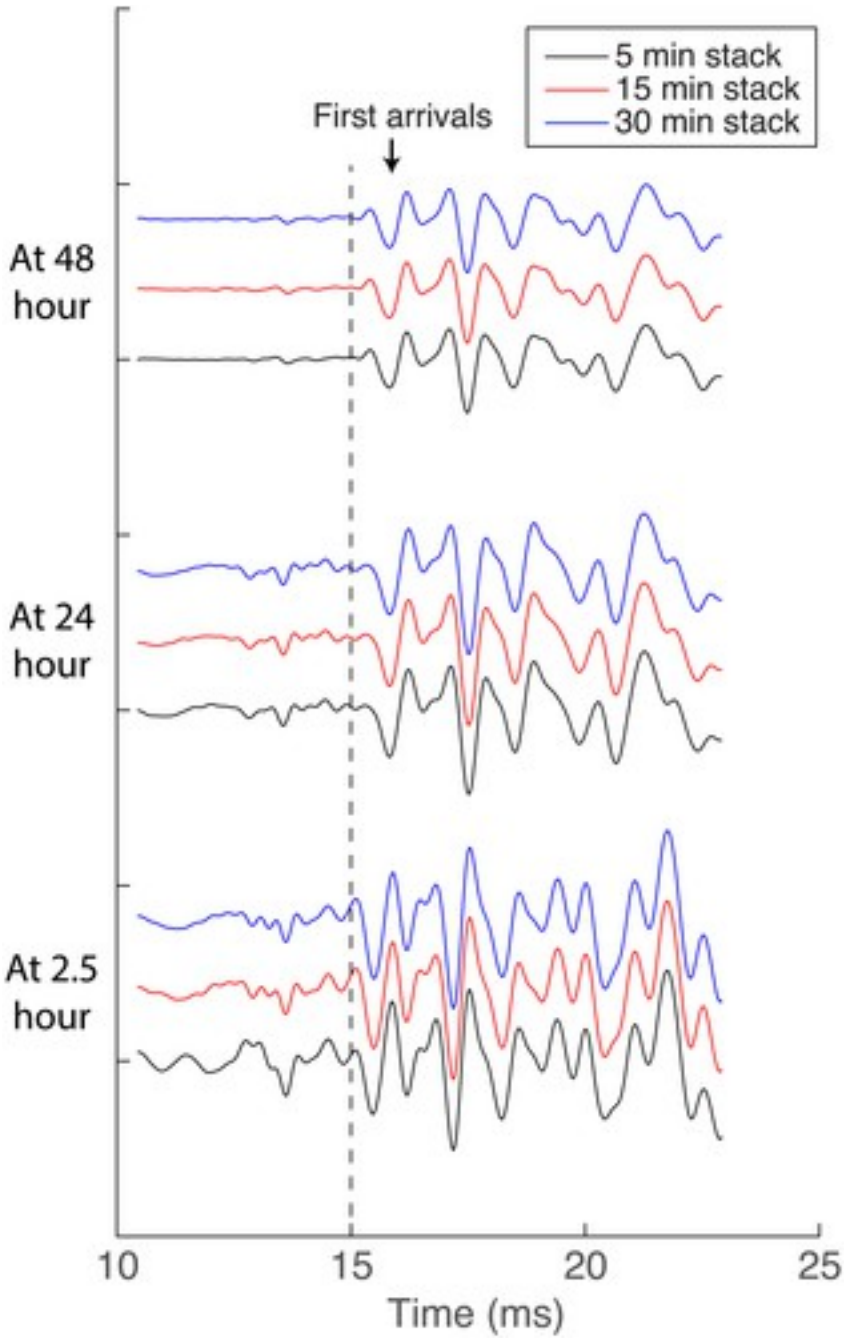

Figure 3

Open in figure viewerPowerPoint

Three stacking intervals: 5 min (black), 15 min (red), and 30 min (blue) at selected elapsed times (2.5 h, 24 h, and 48 h). The example data were recorded at the depth of 1680 m.

Caption

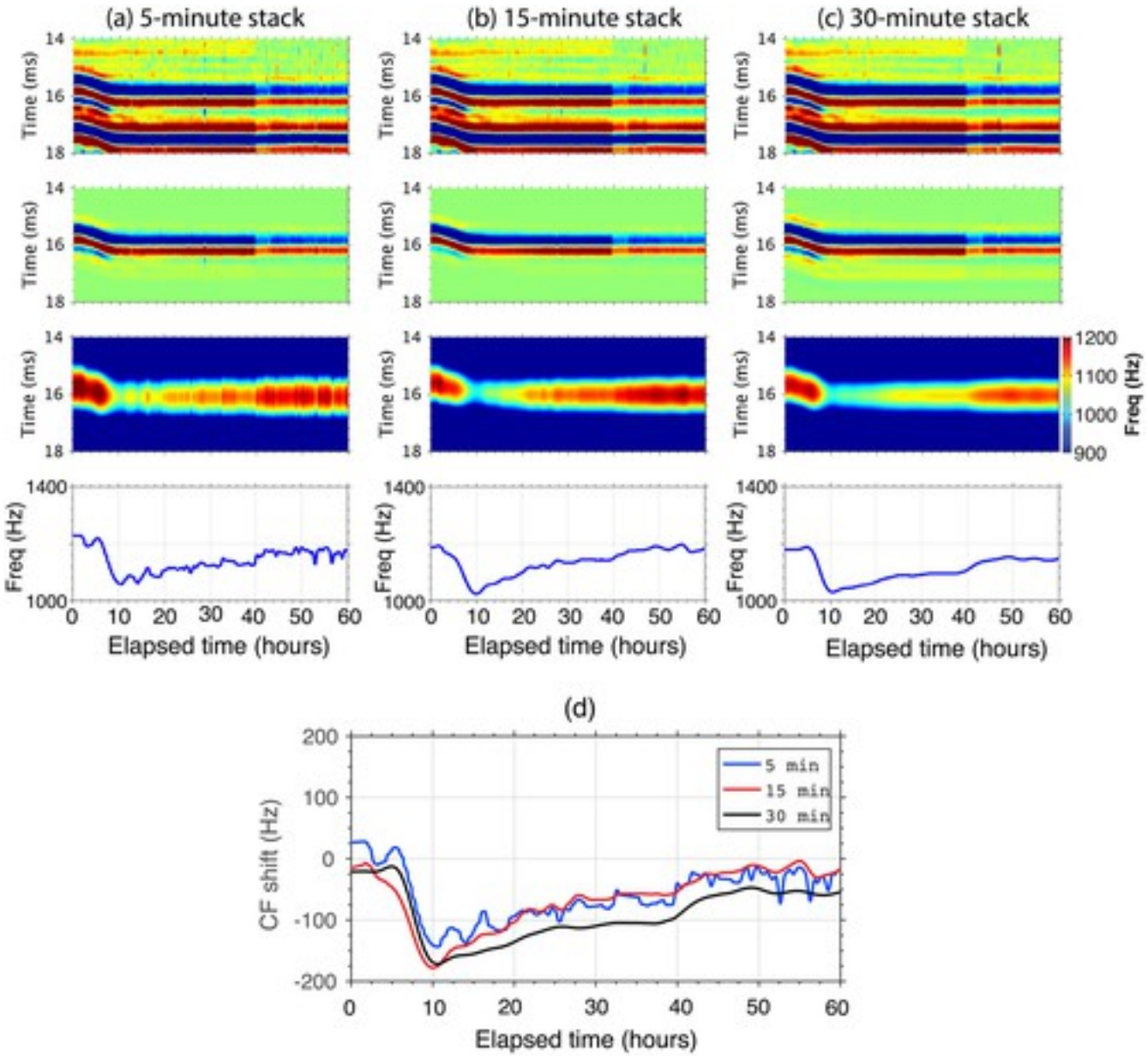

Figure 4

Open in figure viewerPowerPoint

Centroid frequency results from three stacking intervals: 5 min (a), 15 min (b), and 30 min (c). (first row) Raw stacking data. (second row) Data in a first arrival window. (third row) Centroid frequency map of first arrivals with colorscale shown in the right column. (fourth row) Maximum centroid frequency value curve. (d) Centroid frequency shifts for three stacking time intervals.

Caption

Figure 4d shows the centroid frequency shifts relative to the reference CF value for preinjection (calendar time $T = -0.5$ h). It is not surprising that the blue curve (5 min stack) shows the fluctuations. In contrast, the black curve (30 min stack) might be too smooth to preserve possible physical variation during the rapid CO_2 movement. Among three curves, 15 min stack is chosen

for further attenuation analysis. Overall, the three curves show similar trends and small fluctuation of frequency shifts. Our analysis led to the conclusion that selection of an appropriate stacking duration is able to stabilize the frequency shift while measuring a relatively rapid process.

2.5 Choice of Window Length

The second factor, the length of window used for the first arrival, also influences centroid frequency estimates. In this case, we compared three Gaussian windows with different lengths to illustrate how the window size influences the estimation of the centroid frequency. The data with the 15 min stack shown in the first row in Figure 5a is same for three scenarios. In the second row of Figure 5a, the first arrivals are obtained by using three Gaussian windows with lengths of 3.7 ms, 2.6 ms, and 1.8 ms. The window length is defined as the number of nonzeros of the window function in Figure 5b. By using the longer window length the data may include interfering arrivals, whereas the shorter window may truncate the first arrival, shown in the second row of Figure 5a. The third row shows the corresponding centroid frequency maps. The three maps show a common feature: high frequencies sharply decrease to low values and then gradually recover, which is also clearly demonstrated in the bottom row. The difference is that the narrower window seems to result in higher frequencies (see the right plot). The right plot (1.8 ms window) may not be optimal either because information is probably lost with tight cut. Figure 5c shows the centroid frequency shifts with an interesting behavior: before the trough point three curves are quite close, but after the trough point the blue curve (1.8 ms length window) has a larger slope, while the black curve (3.7 ms length window) has a smaller slope. It is likely that these low frequencies (interference waves) compromised of high frequencies of first arrivals. This test suggests that the CF shift trends do not depend strongly on the choice of window length; the magnitude is slightly modified though. To combine our observations of the waveform and CF content of the first arrival, we selected the 2.6 ms Gaussian window in the following calculations.

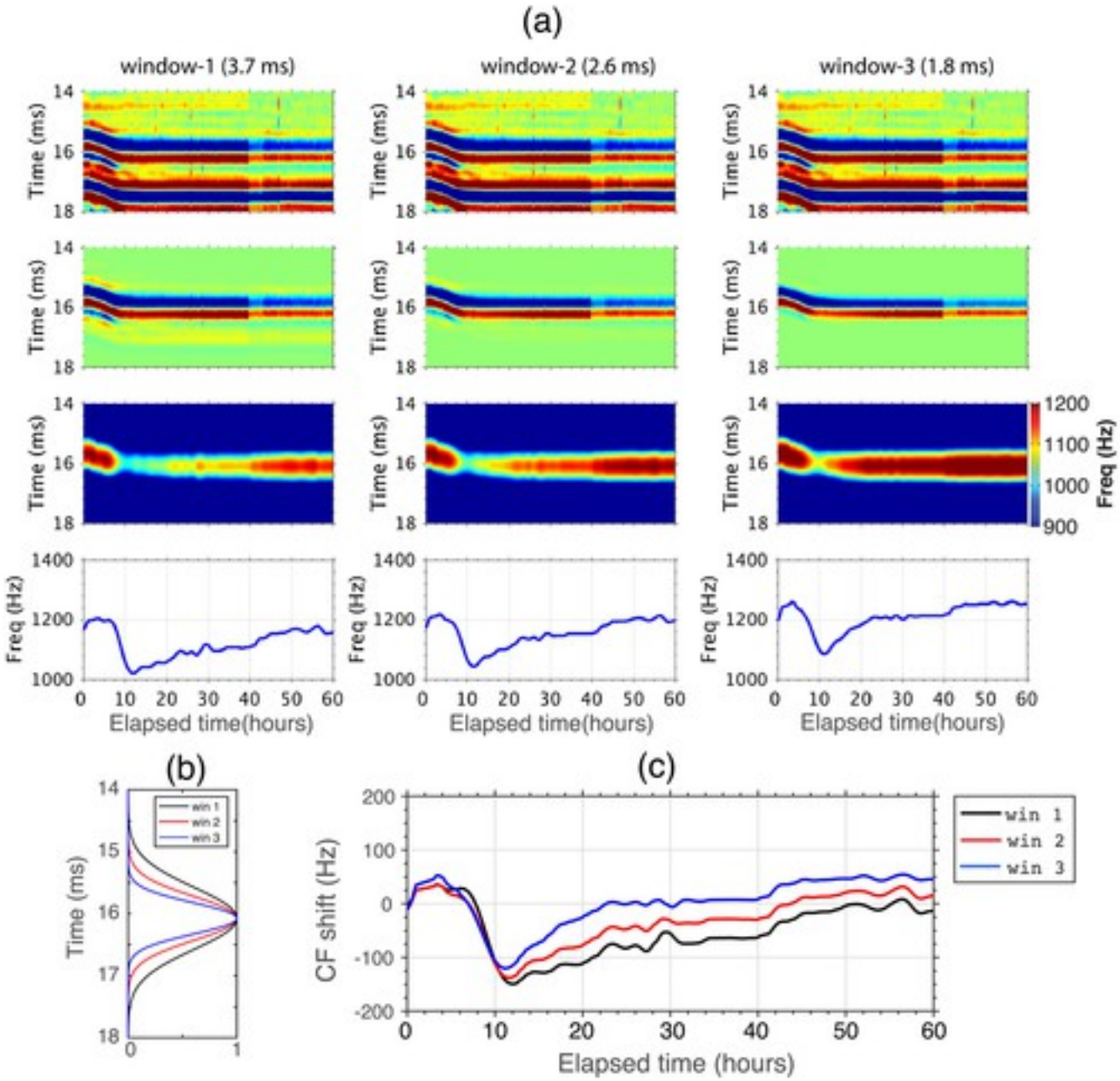

Figure 5

Open in figure viewerPowerPoint

(a) Centroid frequency calculations with different window length: 3.7 ms (window 1), 2.6 ms (window 2), and 1.8 ms (window 3). Four rows represent raw data, windowed first arrivals, centroid frequency map, and maximum centroid frequency value respectively. (b) Three Gaussian windows with three lengths: 3.7 ms (win 1), 2.6 ms (win 2), and 1.8 ms (win 3). The center of the Gaussian window is defined as the first arrival pick that is varying with time elapsed hours. (c) Centroid frequency shifts corresponding to three windows.

Caption

3 Results

3.1 Spatial-Temporal CF Changes

Figure 6 shows the maximum centroid frequency values of the first arrivals as a function of calendar time for six representative sensors, at depths of 1634 m, 1648 m, 1650 m, 1658 m, 1676 m, and 1680 m, from top to bottom. Data from the six sensors can be compared to the schematic raypaths in Figure 1 to show the spatial-temporal relationship of the measured CF and attenuation changes. The deeper sensor (1680 m) shows a sharp drop in the centroid frequency beginning at only 3–4 h after injection with increase after about 10 h. The 1676 m sensor shows a slight decrease in the centroid frequency beginning at about 6 h after injection with increase after about 15 h. The peak frequency shifts are about 200 Hz at the depth 1680 m and about 100 Hz at the depths 1676 m. The 1658 m sensor shows a more gradual decrease in centroid frequency beginning at about 15 h after injection and arriving at about 80 Hz shift at about 22 h. The CF at the 1650 m sensor, which has a raypath along the top of the reservoir, begins to shift up after injection and decreases after about 40 h. The CF shift is up to 360 Hz. At the 1648 sensor (right below the packer), the trend of frequency shift is quite similar to the 1650 m sensor. The CF shift is about 150 Hz. The location of the lowest CF is shifted toward later calendar time in four receivers from 1680 m to 1648 m. The observed centroid frequency shifts of 50 to 200 Hz represent 2% to 20% changes in centroid frequency. Above the packer at 1634 m depth (the top sensor), there is no significant, systematic change in centroid frequency, which was also observed in the first arrival's traveltime curve [*Daley et al*., 2007]. No clear trend in frequency shifts above the packer demonstrates that the below-packer changes are in the subsurface and that the near-source volume has not been affected by the CO_2 injection. We conclude that the observed frequency shifts are real and can be interpreted in terms of CO_2 plume migration and/or saturation changes.

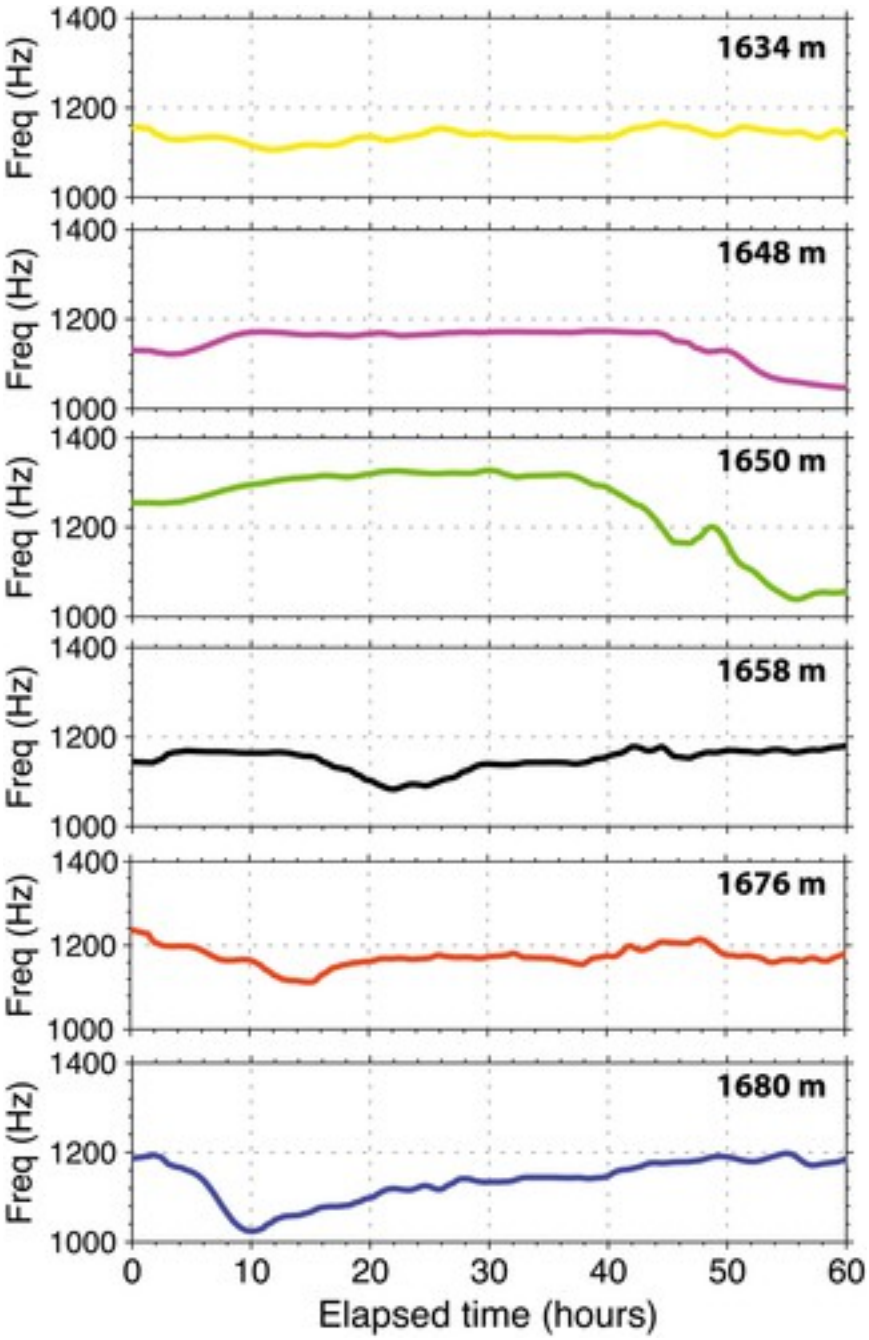

Figure 6

Open in figure viewerPowerPoint

Centroid frequency shifts at different depths of receivers as a function of the elapsed time in 60 h after injection.

Caption

3.2 Spatial-Temporal Attenuation Changes

Temporal attenuation changes are calculated using equation 5 and shown in Figure 7. Ray length *d* for six sensors (top-bottom) are 38.9 m, 32.0 m, 31.46 m, 30.33 m, 32.5 m, and 37.26 m,

respectively. These calculations assume a straight raypath that remains constant during CO_2 injection. Above the packer depth, we do not see systematic attenuation changes shown in the top plot in Figure 7. Because of fixed source and sensor location, waveform differences contain information on temporal variations of the medium in which seismic waves propagated. Temporal variations of attenuation are therefore expected as the result of the temporal variation of CO_2 saturation in the region where the raypath is passing through.

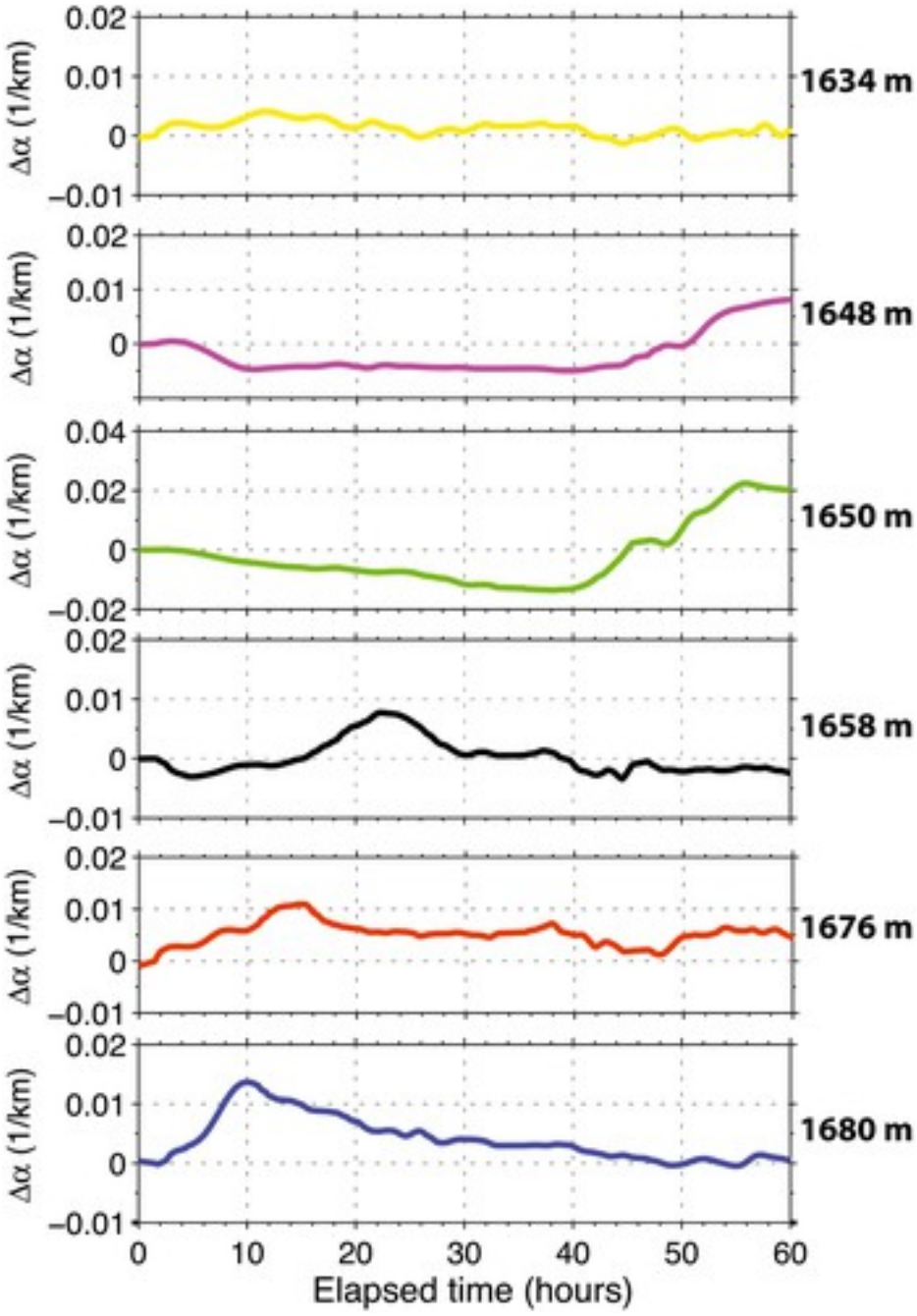

Figure 7
Open in figure viewerPowerPoint

Attenuation changes at different depths of receivers over the elapsed time in 60 h after CO_2injection.
Caption

Below the packer, attenuation changes display four common features:

1. minimal or negative change in attenuation at the beginning of injection (before the CO_2plume moves across the corresponding raypath);
2. different time of CO_2 plume crossing the seismic ray, and
3. a significant increase in attenuation; and
4. attenuation seems to gradually decrease following the peak.

Small attenuation variations (feature 1) are clearly observed at the sensors depths of 1658 m, 1650 m, and 1648 m. At sensors depths of 1650 m and 1648 m, attenuation after injection decreases compared to the preinjection, particularly at the 1650 m sensor. When the CO_2plume moves across the rayfan, sensors show different detection times of the CO_2 plume that could be used to estimate the migration speed of CO_2 plume (feature 2). Attenuation increases to a peak positive value (feature 3) that is likely related to the amount of CO_2 (saturation). The difference in the attenuation change between sensors is likely to reveal heterogeneities in the reservoir. Attenuation decreases (feature 4) as the CO_2 plume continues to migrate. Feature 4 is distinguished from traveltime delay which stabilizes to a maximum time delay [*Daley et al*., 2007]. These features are broadly consistent with the constrained flow models presented in *Daley et al*. [2011].

Next, we focus our analysis on the attenuation changes observed at the depth of 1680 m because of the short delay between the initiation of injection and seismic evidence of CO_2saturation for this raypath. In Figure 8a, the cumulative mass of injected CO_2, as measured by integration of a surface mass flow gauge (red curve), increases, and correspondingly, there is an increase in attenuation in Figure 8c and decrease in velocity in Figure 8b (see gray zone (1)). After approximately 10 h, CO_2 saturation continues to increase; during this period, attenuation change starts to decrease, whereas measured velocity change ($\frac{\Delta V}{V_0} \approx -\frac{\Delta t}{t_0}$, see Appendix Appendix A for derivation) tends to plateau (see gray zone (2)). We noticed that at 40 h there is a small drop in both velocity and attenuation, which might be the response of the injection halt between (40–48 h). When the injection rate recovers, attenuation continues decreasing and velocity change remains flat (see gray zone (3)). This velocity-attenuation relationship can be better illustrated with a crossplot of velocity and attenuation changes (dots) with injection duration, as shown in Figure 10. The color of dots represents the time since the start of injection. Velocity and attenuation changes increase quickly in the first 10 h and reach a peak (~14% attenuation change

and ~2.5% velocity change). Then attenuation change sharply drops to zero, while velocity change slightly oscillates around ~2.5%.

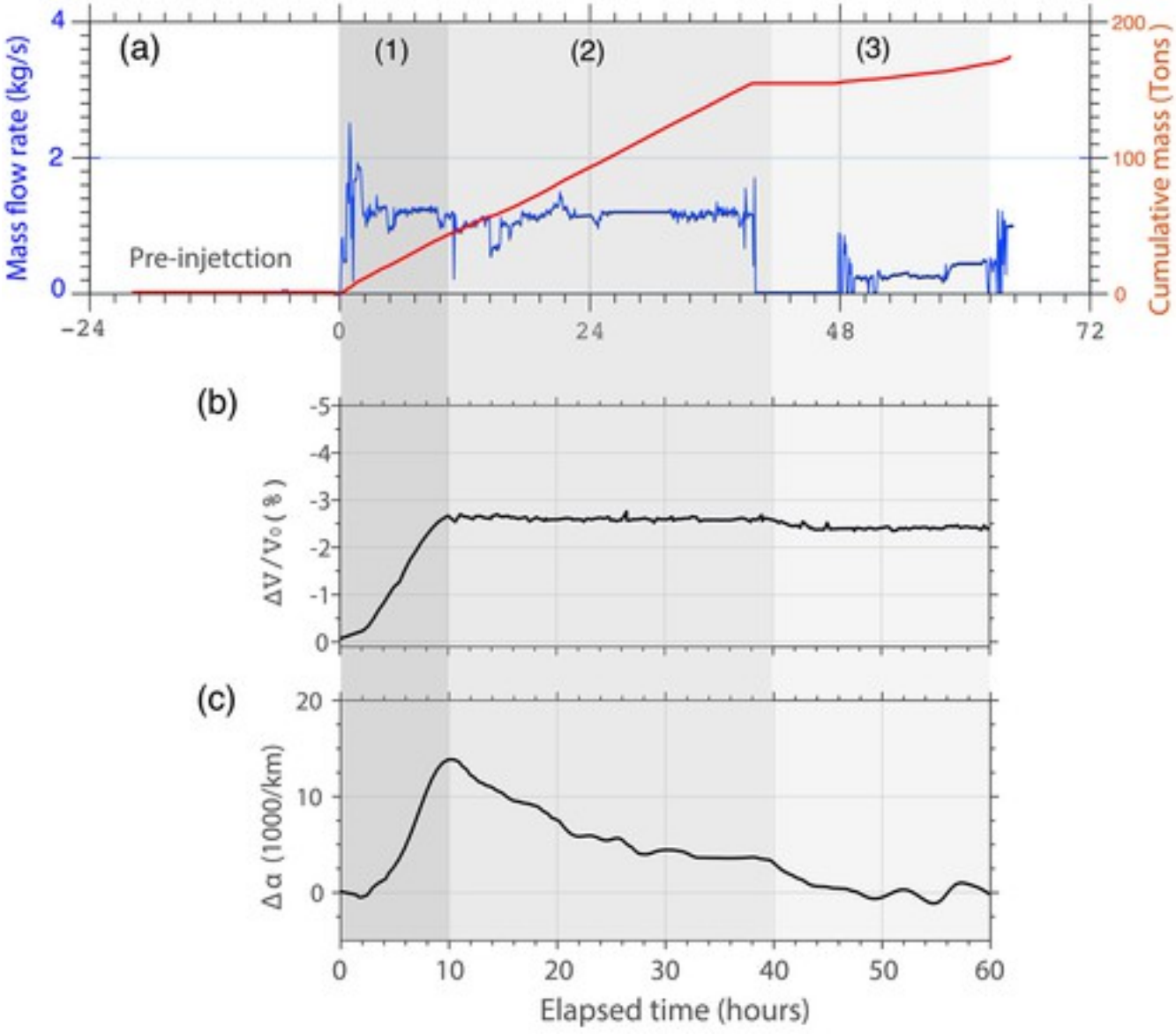

Figure 8

Open in figure viewerPowerPoint

(a) The injection rate (mass flow) measured in the injection well (blue) and cumulative mass of CO_2 (red) calculated by taking the integral of mass flow with increasing time. (b) Observed velocity change relative to velocity (V_0) before injection at the 1680 m sensor. (c) Calculated attenuation change varying with the elapsed time (injection hours) at the 1680 m sensor.

Caption

Next, we will use in situ measured CO_2 amount, rock physics theory, and White's attenuation model together to explain details of the four features discussed previously.

3.3 Interpretation Using White's Patchy Saturation Model

A wealth of prior laboratory studies demonstrate that seismic attenuation is sensitive to both fluid saturation and pressure [*Nur and Simmons*, 1969; *Johnston and Toksöz*, 1980]. Fluid saturation increases the attenuation of body waves due to a variety of proposed mechanisms including fluid flow in or between cracks (e.g., squirt mechanisms), direct Biot dissipation, and relative fluid flow across patch boundaries in multiphase saturation scenarios. Increasing pore pressure typically leads to an increase in attenuation, likely due to the opening of compliant cracks. During the Frio II field pilot, the maximum observed pore pressure increase was only 0.28 MPa with a starting overburden pressure of 16.5 MPa, corresponding to a relatively small (<2%) effective stress variation. Given the low stress sensitivities of rocks at initially high effective stress states, the observed attenuation changes are likely caused by changes in CO_2saturation during injection, rather than increasing pore pressure.

During the experiment, the temporal variation in the amount of CO_2 at the observation well was measured directly using fluid sampling via a U-tube [*Freifeld et al*., 2005]. These measurements quantify the fraction of CO_2 in the mixed gas phase in the observation well. This measurement provides a constraint on plume break-through time between the two wells independent of seismic measurements. We selected White's patchy saturation model to describe *P* wave attenuation due to the two-phase flow of brine and CO_2 relative to the porous rock frame (CO_2 and brine) [*White*, 1975; *Dutta and Seriff*, 1979]. The elastic properties of the rock frame were selected from log and core information collected in the Blue sand formation (base V_p = 2700 m/s, base V_s = 1200 m/s, density 2200 kg/m^3, porosity = 25%, and permeability = 2 darcies) [*Daley et al*., 2011]. CO_2 and brine properties, shown in Table 1, were calculated for in situ reservoir pressures and temperatures (P = 16 MPa, T = 55°C) using the *Batzle and Wang*'s [1992] equations. We assume that the initial fluid is a mixture of brine (97%) and gas (3%) in solution. All *P* wave velocity and attenuation calculations were made assuming a seismic frequency of 1000 Hz, an appropriate value based on spectral analysis of our CASSM data. All fluid properties are listed in Table 1.

Table 1. Brine-CO_2 Petrophysical Properties Calculated by Baztle-Wang Relation Under the Condition: Water Salinity = 100,000 ppm, Gas Gravity = 0.75, Gas-Brine Ratio = 0, Temperature = 55°C, and Pressure = 16 MPa

Fluids	Velocity (m/s)	Density (kg/m^3)	Viscosity (cPs)
Brine	1643	1048	0.67
Gas	435	156	0.02
CO_2	275	620	0.02

As has been discussed in the literature, the seismic response during CO_2 injection is determined by both the CO_2 saturation as well as the characteristic length scale of CO_2 within the system, often termed the patch dimension in patchy saturation models [*Lei and Xue*, 2009; *Caspari et al*., 2011; *Ajo-Franklin et al*., 2013]. White's model assumes that these patches are spherical in shape. Past estimates of $scCO_2$ characteristic patch sizes from laboratory and field measurements vary but are generally in the millimeter to centimeter range; *Caspari et al*. [2011] report characteristic patch sizes of 1–5 mm from analysis of well logs at the Nagaoka site, while *Nakagawa et al*. [2013] estimate patch dimensions of 1 cm from laboratory resonance experiments. Based on flow simulations of an outcrop analogue reservoir, *Kirstetter et al*. [2006] estimate fluid-patch sizes for different production scenarios; e.g., water displaces oil to be on the order of 1 m. Based on the White model, we will fit both velocity and attenuation measurements to determine the patch size range. We should note that this analysis effectively treats each raypath as a homogeneous zone with a single “mean” saturation along the raypath and patch size; this simplification is required in the absence of sufficient ray coverage to allow effective imaging, and the resulting estimates are likely less precise than would be available for a full tomographic survey.

Here we test different patch sizes in the White model, over a sequence of values (30, 50, 70, and 90 cm) to best fit velocity-attenuation measurements. Figure 9 shows predicted velocity change (Figure 9a) and attenuation change (Figure 9b) together with theoretical Gassmann-Reuss and Gassmann-Voigt bounds, which are predicted by the Gassmann fluid substitution with the fluid bulk modulus computed by Reuss (or Wood) and Voigt (or Hill) averages of two fluids [*Mavko and Mukerji*, 1998; *Toms et al*., 2006]. The maximum *P* wave attenuation $\Delta\alpha/\alpha_0$values predicted by White's model quantitatively match with measured attenuation values in Figure 8c in terms of

magnitude, thus increasing our confidence in the appropriateness of the model. The α_0 is the reference attenuation value before injection (at injection time 0) and is estimated using equation 2, in which the source frequency is chosen as 1300 Hz greater than the receiver frequencies. The predicted maximum *P* wave velocity change

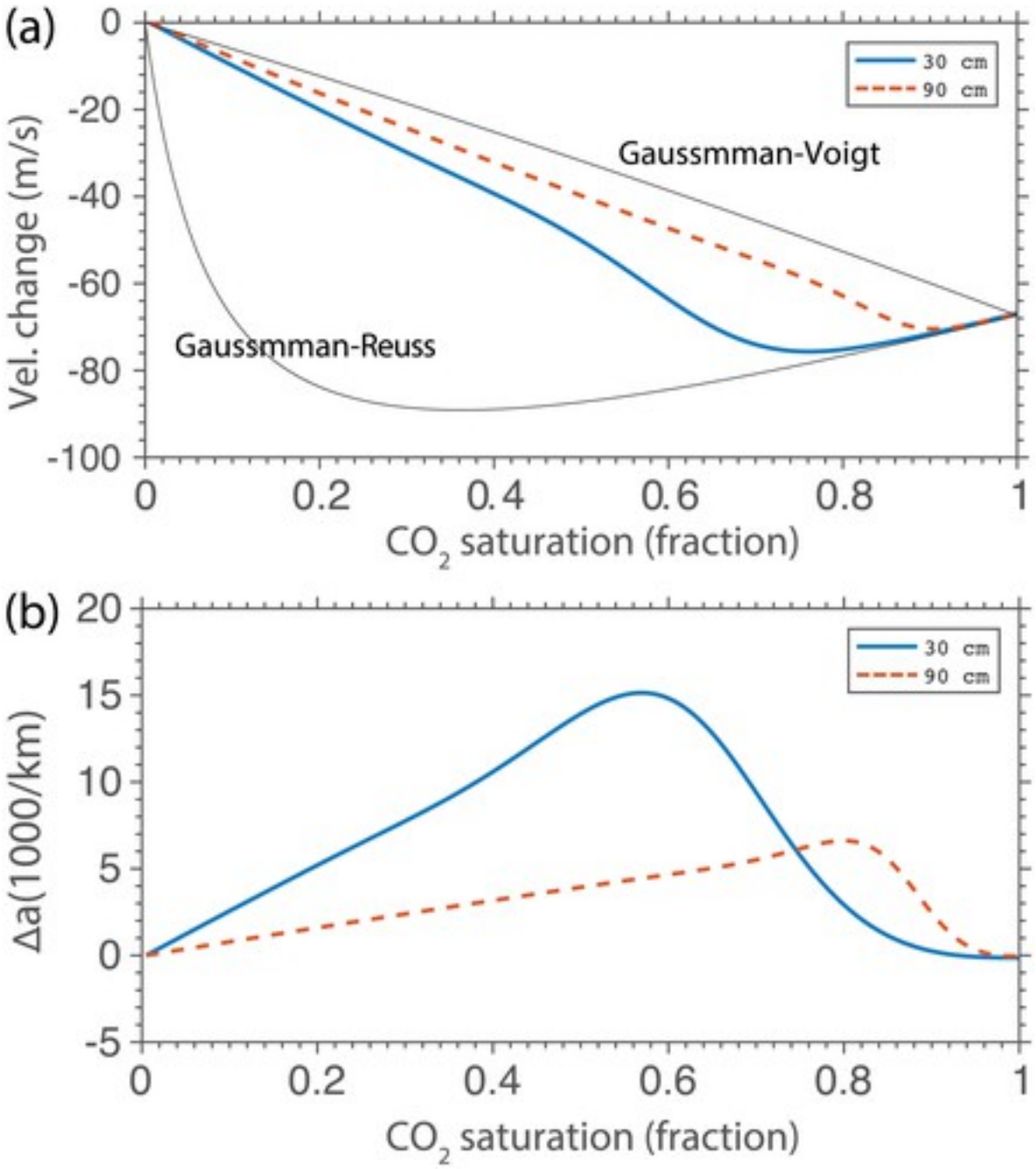

Figure 9

Open in figure viewerPowerPoint

(a) Predicted velocity change and (b) attenuation change using two patch size models (30 cm and 90 cm) in comparison to the Gassmann-Reuss lower bound and Gassmann-Voigt upper bound.

Caption

$$\frac{\Delta V}{V_0} \approx \frac{-70}{2700} \approx -2.6\%$$

also can match with measured velocity change in Figure 8b.

We overlay predicted velocity-attenuation curves from White's model on the CASSM measurements (dots) in Figure 10. In a general sense, smaller patch sizes yield larger attenuation changes. Velocity change seems to less sensitive to the patch size than attenuation change. The patch sizes from 90 cm (purple) to 50 cm (blue) give a reasonable fit to the measurements (dots). At the peak variation in *P* wave velocity and attenuation (~10 h), CO_2saturations in the modeled trajectory are in the vicinity of 70%, well beyond the saturation values viewed as the sensitivity limit in prior studies. Saturation values in this range are, however, consistent with prior $scCO_2$ saturation estimates acquired at the site using a reservoir saturation tool during the earlier Frio 1 experiment, which utilized the higher Frio C sandstone [*Hovorka et al.*, 2006]. While this increased sensitivity to saturation is partially due to the more linear relationship between velocity and saturation in White's model with respect to CO_2 saturation at crosswell frequencies, the addition of attenuation also increases sensitivity to CO_2 saturations near 70%. After the peak, attenuation change sharply drops as the best matching patch size increases sharply from 30 cm to 90 cm. This variability could suggest either a temporally varying patch size or a larger macroscopic $scCO_2$ redistribution due to buoyancy. Finally, we overlay measured velocity-attenuation data from two other sensors (1658 m and 1676 m) to Figure 10, shown in Figure 11. The shape of the blue curve at 1676 m are similar to that at 1680 m. The purple curve with the patch size of 90 cm gives better match to the data from 1676 m. The red curve (30 cm patch size) matches very well the first half curve of 1658 m sensor which has a different shape from the other two. None of the models can fit the second half curve of 1658 m, which may imply temporally varying patch size from 30 cm to 90 cm or toward a more complicated buoyancy-driven $scCO_2$ redistribution.

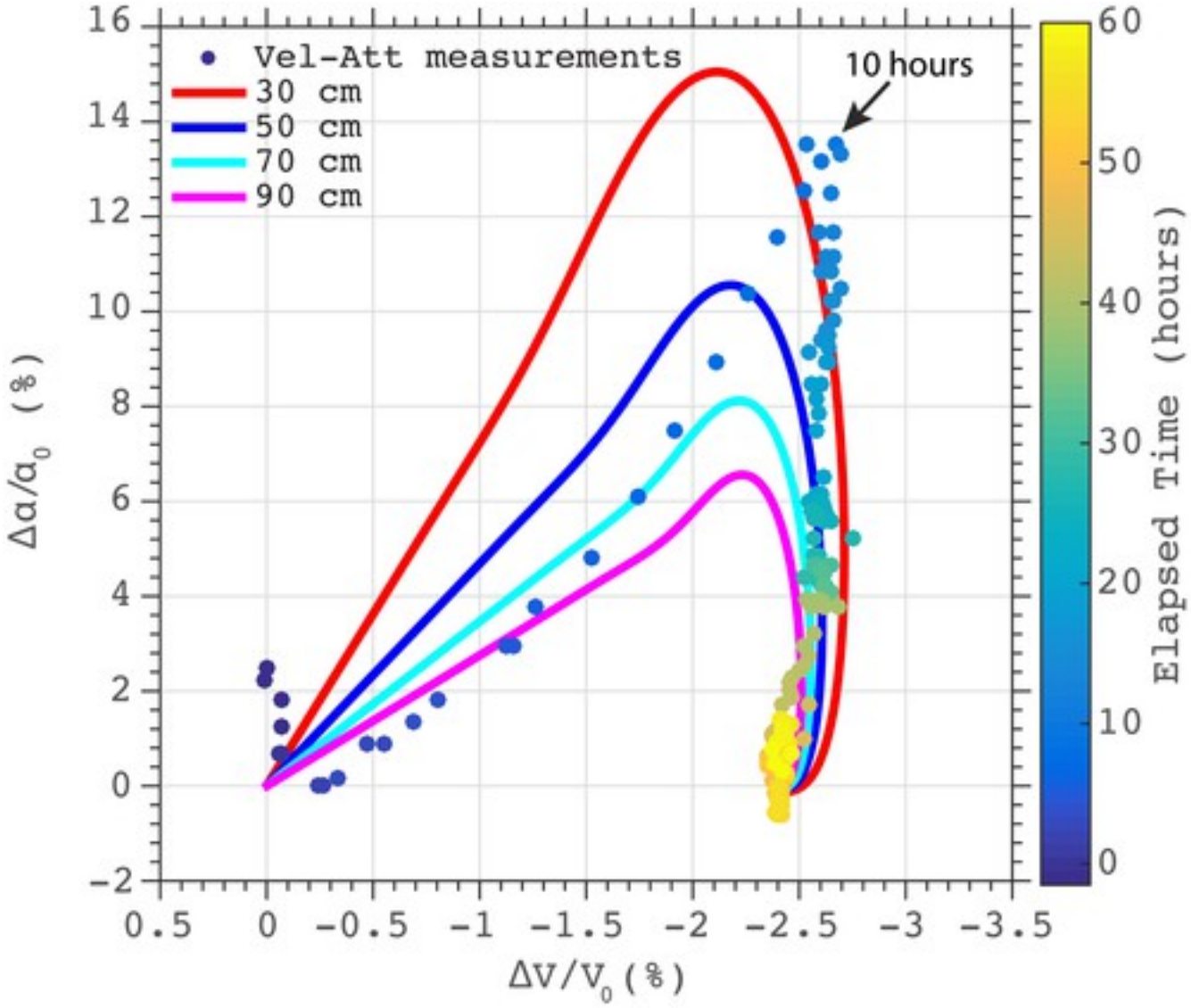

Figure 10

Open in figure viewerPowerPoint

Crossplots of measured velocity ($\Delta V/V_0$) and attenuation change ($\Delta\alpha/\alpha_0$); α_0 is computed by equation 2 where the source frequency is assumed as 1300 Hz during CO_2 injection at the 1680 m depth sensor in the Frio site. The color bar indicates hours elapsed since the start of injection. The overlaid color lines are prediction values using the White's model with a variety of the patch sizes: 30 cm, 50 cm, 70 cm, and 90 cm.

Caption

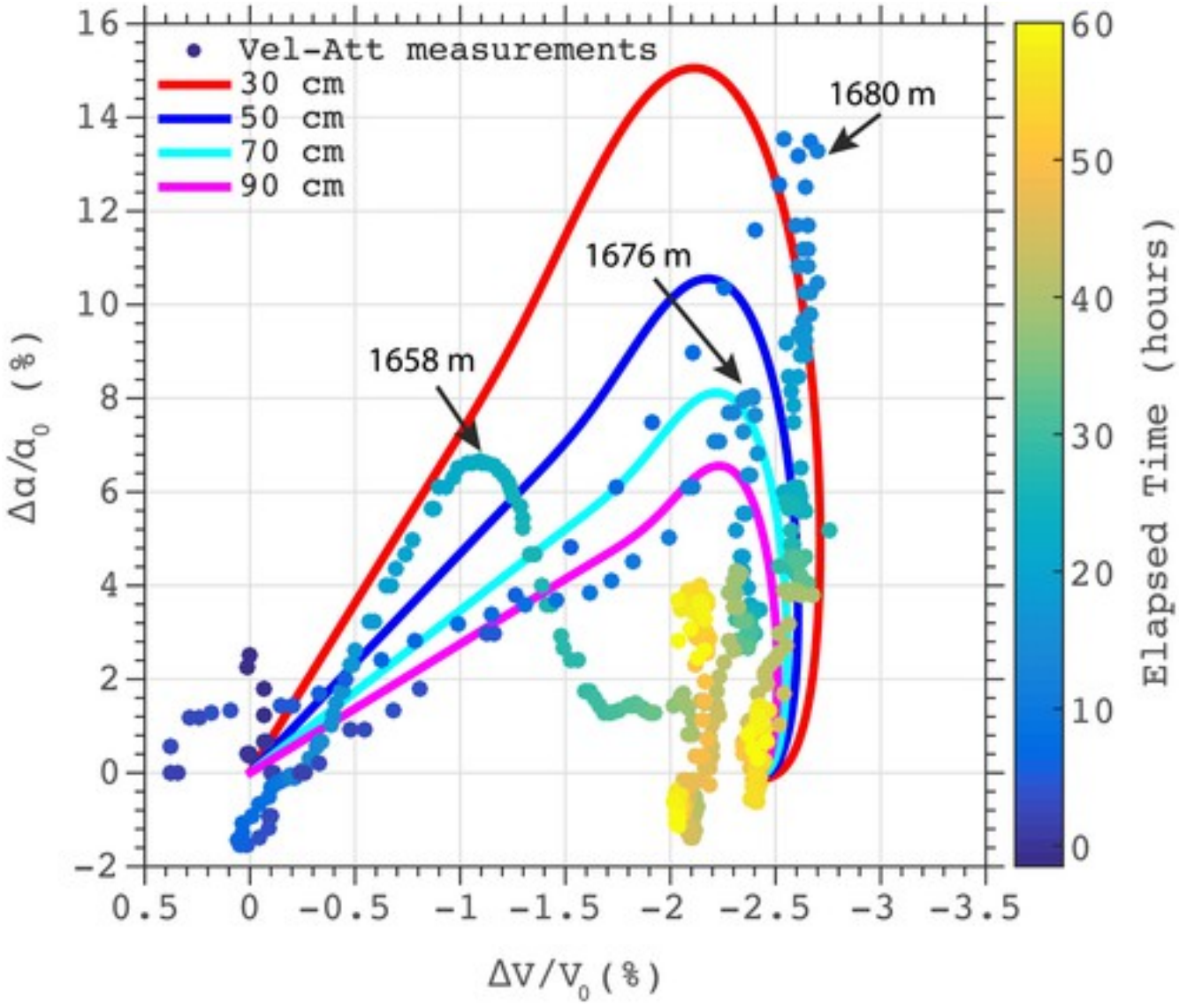

Figure 11

Open in figure viewerPowerPoint

Crossplots of measured velocity change ($\Delta V/V_0$) and attenuation change ($\Delta\alpha/\alpha_0$) during CO_2injection at the 1680 m, 1676 m, and 1658 m depth sensors in the Frio site. The color bar indicates injection hours. The overlaid color lines are prediction values using the White rock physics model with the patch size: 30 cm, 50 cm, 70 cm, and 90 cm.

Caption

We should note that the use of White's model in this case is on the edge of validity for patches sizes of 90 cm. The model requires patches to be well below a seismic wavelength; given a *P*wave velocity of 2700 m/s and a mean frequency of 1 kHz, our wavelength is ~2.7 m, three times larger than a patch at 90 cm. At these scales, scattering could become a competing effect, independent of patch-based flow mechanisms. However, given the match observed in attenuation magnitudes, we do not need to appeal to scattering to provide a reasonable explanation of observed attenuations.

4 Discussion

This is the first investigation of spatiotemporal attenuation changes during CO_2 injection using active source seismic data. Our study highlights the potential of attenuation changes to indicate the movement of CO_2 replacing brine in the pore space. As the CO_2 plume migrates, we observe that attenuation first increases and then reaches the peak value. Attenuation variations at spatially distributed sensors could reveal the movement and distribution of CO_2plumes within the reservoir, which is complementary to time delays of first arrivals. As the CO_2plume continues to migrate, interestingly, attenuation decreases. This is distinguished from velocity (traveltime) change that remains flat after a critical time point. We believe that decreasing attenuation is related to increasing saturation or temporally varying patch size, as discussed in the interpretation section. We have developed a crossplot technique for velocity and attenuation changes that allows us to estimate patch size from a patchy-saturation model.

The amount of seismic attenuation change seen in various raypaths provides information about the heterogeneous distribution of the CO_2 plume that is very important for fluid migration. Such heterogeneity needs to be well understood and characterized. Multiple sensors agree on the temporal changes in attenuation, but we cannot spatially image with the single source CASSM data. More sources can lead to better spatial imaging as demonstrated by *Ajo-Franklin et al*. [2011] with multilevel CASSM.

This study also reminds us of the limitations of sparse time-lapse attenuation changes for inverting CO_2 saturation. For example, two possible CO_2 saturation scenarios could lead to equal attenuation change (see Figure 8) due to the fact that the attenuation model is not single valued. Continuous monitoring of seismic attenuation using repeated active sources can partially remedy the problem and would provide important insights into the dynamic state of a CO_2 plume. Also, CO_2 reservoirs will benefit from an effective continuous seismic monitoring strategy to ensure efficient and timely management decisions [*Arogunmati and Harris*, 2012, 2014].

While neither seismic velocity nor attenuation uniquely determine CO_2 saturation and patch dimensions [*Zhang et al*., 2015], the combination of the two, particularly for midsaturation levels, can improve estimates, particularly in cases where patchy mechanisms are dominant, which is also suggested by experimental observations in ultrasonic velocity and attenuation [*Lei and Xue*, 2009]. In situations outside of this regime, the addition of nonseismic measurements (e.g., electrical resistivity tomography or crosswell electromagnetic surveys) may be necessary to improve quantitative saturation estimation; e.g., resistivity is considered to be sensitive to $scCO_2$ in large range from experimental studies [*Xue et al*., 2009; *Kim et al*., 2011]. The same

principles can be applied to the case of oil reservoirs with partial gas saturation or in EOR scenarios.

5 Conclusions

We have extracted information on the spatiotemporal attenuation changes from the first arrivals of crosswell continuous active-source monitoring data at the Frio CO_2 sequestration site. The amount of seismic attenuation change induced by CO_2 injection is interpreted as a function of CO_2 saturation and characteristic patch length scale. In the temporal dimension, attenuation has an immediate increase at the beginning of injection (small CO_2 saturation) as seismic velocity decreases. This phenomenon suggests that a small amount of leaked CO_2might be detected by observing the change in both seismic velocity and attenuation. As injection continues, attenuation decreases, likely due to saturation increase or patch size increases, based on White's attenuation model. In the spatial domain, the amount of seismic attenuation change for various raypaths provides information about the macro as well as subscale distribution CO_2 in the plume, aspects important for constraining fluid migration. We have combined the velocity and attenuation change data in a novel crossplot format that is useful for model-data comparison and determining patch size. Using the White patchy-saturation model to fit velocity-attenuation measurements, we estimate the range of patch size in the injection zone as 30 cm to 90 cm. The patch size and CO_2 saturation vary across the sensors (spatial variation) and is also a function of injection time. The findings suggest that attenuation changes are physically caused by CO_2 movement and saturation variation and that spatiotemporal seismic attenuation measurements by CASSM could be a suitable tool to monitor these processes.

Seismic attenuation change presents an additional constraint to quantify the CO_2 saturation. More detailed analyses, such as quantitative inversion of the CO_2 saturation, are possible in future work and will be enhanced by these results.

Acknowledgments

We thank the anonymous reviewers for critical comments. We wish to thank Sergey Fomel for the help of data processing using Madagascar [*Fomel et al*., 2013]. This study was supported by the startup funding from Department of Geosciences and Institute of Natural Gas Research at the Pennsylvania State University. Seismic data used in this study is owned by the U.S. Department of Energy (DOE) and Lawrence Berkeley National Lab (LBNL) and can be accessed with the permission from LBNL (https://eesa.lbl.gov/departments/geophysics/). The field work was supported by the GEOSEQ project, along with LBNL work supported by the Assistant Secretary

for Fossil Energy, Office of Coal and Power Systems through the National Energy Technology Laboratory, of the U.S. DOE, under contract DE-AC02-05CH11231. Secondary support for J. Ajo-Franklin was provided by U.S. DOE, Office of Science, Office of Basic Energy Sciences, Chemical Sciences, Geosciences, and Biosciences Division under DE-AC02-05CH11231.

Appendix A: Calculate Velocity Change From Observed Traveltime Change

Assume a homogeneous medium, we define baseline velocity V_0 before injection and the perturbed velocity ΔV is the velocity after injection V_1 minus the baseline velocity V_0 ($\Delta V = V_1 - V_0$). Similarly, t_0 , t_1 are traveltimes of the first arrival in the baseline survey and the repeat survey, respectively, so $\Delta t = t_1 - t_0$. Thus, the velocity change is

$$\frac{\Delta V}{V_1} = \frac{V_1 - V_0}{V_1} = \frac{d_1/t_1 - d_0/t_0}{d_1/t_1}$$

Assume that small velocity change would not influence the ray travel length much, so the ray length for before and after injection $d_1 \approx d_0$.

$$\frac{\Delta V}{V_1} = \frac{d_1/t_1 - d_0/t_0}{d_0/t_1} \approx \frac{\frac{1}{t_1} - \frac{1}{t_0}}{\frac{1}{t_1}} = \frac{t_0 - t_1}{t_0} = -\frac{\Delta t}{t_0}$$

Due to the fact $\Delta V \ll \min(V_0, V_1)$, so $\frac{\Delta V}{V_1} \approx \frac{\Delta V}{V_0}$. Thus, we have $\frac{\Delta V}{V_0} \approx -\frac{\Delta t}{t_0}$.